Serpentine Mineral Replacements of Natural Olivine and their Seismic Implications: Oceanic Lizardite versus Subduction-Related Antigorite

FRANÇOISE BOUDIER[1]*, ALAIN BARONNET[2] AND DAVID MAINPRICE[1]

[1]GEOSCIENCES, UNIVERSITY OF MONTPELLIER II, PLACE EUGÈNE BATAILLON, 34095-MONTPELLIER, FRANCE

[2]UNIVERSITY OF AIX–MARSEILLE AND CINAM–CNRS, CAMPUS LUMINY, CASE 913, 13288-MARSEILLE, CEDEX 9, FRANCE

We report on microstructural data obtained by optical microscopy and transmission electron microscopy concerning the crystallographic relationships of serpentine minerals with their host olivine in two contrasting situations. In the first case, mesh-textured lizardite (liz) is developed in a standard 60% serpentinized oceanic harzburgite from the Oman ophiolite where olivine converts to columnar lizardite. The joined columns are perpendicular to the basal plane $(001)_{liz}$, corresponding to the pseudofibres observed optically. The plane $(001)_{liz}$ is locally parallel to the narrow boundary ol–liz; thus column orientations register the interface of serpentinization. The ol–liz relationships are not strictly topotactic, but reflect preferred cracking orientations in olivine, parallel to $(010)_{ol}$. In the second case, antigorite (atg) develops in a rare sample of antigorite schist in a kimberlite from Moses Rock (Colorado Plateau), representative of a suprasubduction-zone mantle wedge. High-resolution transmission electron microscopy (HRTEM) images along $[010]_{atg}$ show domains of very regular modulation with a 43·5 Å wavelength ($m = 17$, where m is the number of silicate tetrahedra along the wave), with few defects, indicative of HP–HT antigorite, and also heavily kinked regions as fingerprints of strong tectonic shear. TEM imaging and electron diffraction patterns reveal two topotactic relationships between antigorite and olivine: $[100]_{atg}//[010]_{ol}$ and $<100>_{atg}//<100>_{ol}$; the planes in contact are $(001)_{atg}//(100)_{ol}$ and $(001)_{atg}//(010)_{ol}$, respectively. The $[010]_{atg}//[001]_{ol}$ and antigorite lamellae are parallel to the forsterite b-axis. In both cases, the topography of olivine–serpentine interfaces is controlled by open fluid pathways along microcracks oriented according to the anisotropy of the olivine aggregate. In the cases studied, the serpentine aggregate exhibits a preferred orientation inherited from that of the peridotite. These results have some relevance to the seismic anisotropy of serpentinized mantle. Anisotropy of propagation of seismic waves as a result of the olivine fabric is maintained and reinforced with the development of lizardite. Conversely, the development of antigorite produces a trench-parallel fast S-wave polarization and an anisotropy that is lowered at low degrees of serpentinization and then increased with increasing serpentinization.

INTRODUCTION

Serpentine minerals are receiving increasing attention as an expression of hydration in the mantle and the water cycle in the deep Earth. Serpentine may develop from water penetrating the mantle by cracking in the brittle regime of the oceanic lithosphere at temperatures below 500–600°C. It may develop also from water stored in the mantle above the conditions of maximum stability of serpentine, either as a result of deep hydrothermal circulation in the cooling oceanic lithosphere at spreading oceanic ridges or as a result of slab dehydration below the mantle wedge overlying a subducting plate. In these situations,

*Corresponding author.
E-mail: Francoise.boudier@gm.univ-montp2.fr

we need to understand how water is stored (or circulating) in the mantle before being incorporated in serpentine. One approach is to explore the earliest initiation of serpentinization by studying the topologic and crystallographic relationships between serpentine and its olivine host. This will allow investigation of the possible links between the primary olivine fabric in the mantle and the resulting serpentine network, and subsequently the anisotropy of physical properties, particularly seismic properties.

In this study, we report on the results of optical and electron microscopic (scanning and transmission electron microscopy) studies of two selected samples of partly serpentinized peridotite that are representative of two distinct tectonic situations for which the geometrical relationships between the serpentine mineral and the host olivine could be precisely measured: oceanic lithosphere close to a spreading ridge axis, and a region of subduction-related mantle wedge.

ANALYTICAL TECHNIQUES
Transmission electron microscopy (TEM)

The electron transparent foils for TEM analysis were prepared by Ar^+ ion milling (PIPS–Gatan) at grazing incidence ($7°$ and then $4°$) of a disk extracted from a petrographic $30\,\mu m$ thin section glued to a glass mount with CrystalBond adhesive. A $10\,nm$ thick carbon film was then evaporated onto the specimen surface to ensure electrical conduction.

Conventional transmission electron microscopy (CTEM)

CTEM was performed using the JEOL JEM 2000fx at the facility for electron microscopy, CINaM. It was equipped with a $2.85\,Å$ resolution objective lens and operated at $200\,kV$ acceleration voltage. A $±40°$ double-tilt specimen stage was used for correct crystallographic alignment of antigorite–olivine pairs suitable for imaging and recording the microdiffraction pattern. Images were produced in bright-field mode using low-frequency reflections only, including modulation satellites around $00±1$ only for antigorite in [0l0] orientation.

High-resolution transmission electron microscopy (HRTEM)

HRTEM was performed with the JEOL JEM 30l0 at the facility for electron microscopy, CINaM. The microscope was equipped with a large-gap pole-piece, $2.1\,Å$ resolution objective lens, and operated at $300\,kV$. A $±27°$ double-tilt, eucentric specimen stage was used for careful crystallographic alignment. The high-resolution image in Figure 6 (below) was recorded in axial bright-field mode using a recombination of diffracted beams enclosed in the objective aperture cutting just beyond the resolution frequency. The focus of the objective lens was tuned while collecting a $140\,000×$ to $400\,000×$ magnified image in electron low-dose mode with a LHESA low-light analog camera. Once a suitable image was obtained without drift in very thin area, the full beam was then re-established to record the image on film with less than $2\,s$ of exposure. Eventually, the processed film was scanned at high optical resolution ($1800\,dpi$) in the regions of interest with a Nikon Super Coolscan 8000 SD scanner.

Electron back scattering diffraction (EBSD)

Electron back scattering diffraction (EBSD) maps and pole figures were obtained using by scanning electron microscopy (SEM) on thin sections that were carefully mechanically–chemically polished with diamond pastes of decreasing grain size and finished with an alkaline solution of colloidal silica. The analyses were carried out at the SEM–EBSD facilities at Geosciences Montpellier, Université de Montpellier II (France), using a JEOL JSM 5600 scanning electron microscope with an attached Nordlys-HKL-Oxford digital CCD camera. The main setup parameters were the following: tilt angle of $70°$, working distance of $24\,mm$, accelerating voltage of $17\,keV$, spot size of $83\,\mu m$ and a minimum/maximum number of detected bands on EBSPs of 4/7. Because of the strong alteration of the studied specimens, the mean angular deviation (MAD) for measurements was $2°$, to integrate as many points as possible in olivine grains. However, the pole figures were plotted with an MAD of $1.3°$ of one orientation measurement per detected grain, to increase the data precision and to avoid overestimation of the orientation of large olivine crystals.

LIZARDITE FROM PERIDOTITE IN THE OMAN OPHIOLITE
Optical and fabric measurements

All peridotites from the shallow suboceanic mantle are affected by serpentinization, the extent of which, based on correlation with density measurements (Christensen, 1966), clusters between 30 and 60% for drilled samples from Hess Deep (Iturrino & Christensen, 1990) and for samples collected in Oman (Dewandel *et al.*, 2003).

The upper mantle peridotites in the Oman ophiolite, as well as those exposed or drilled at shallow depth (some hundreds meters) below the ocean floor of the Hess Deep near the East Pacific Rise (Gillis *et al.*, 1993), and in the MARK area on the Mid-Atlantic Ridge (Mével *et al.*, 1991), exhibit a primary fabric inherited from asthenospheric plastic flow recorded by crystal preferred orientation (CPO) of olivine (Fig. 1), and a subsequent fabric related to a penetrative serpentine–lizardite network (Dewandel *et al.*, 2003).

Dewandel *et al.* (2003) explored the possible relationships of the penetrative lizardite network to the primary olivine CPO in a harzburgite sample (97OAl29) that is the object
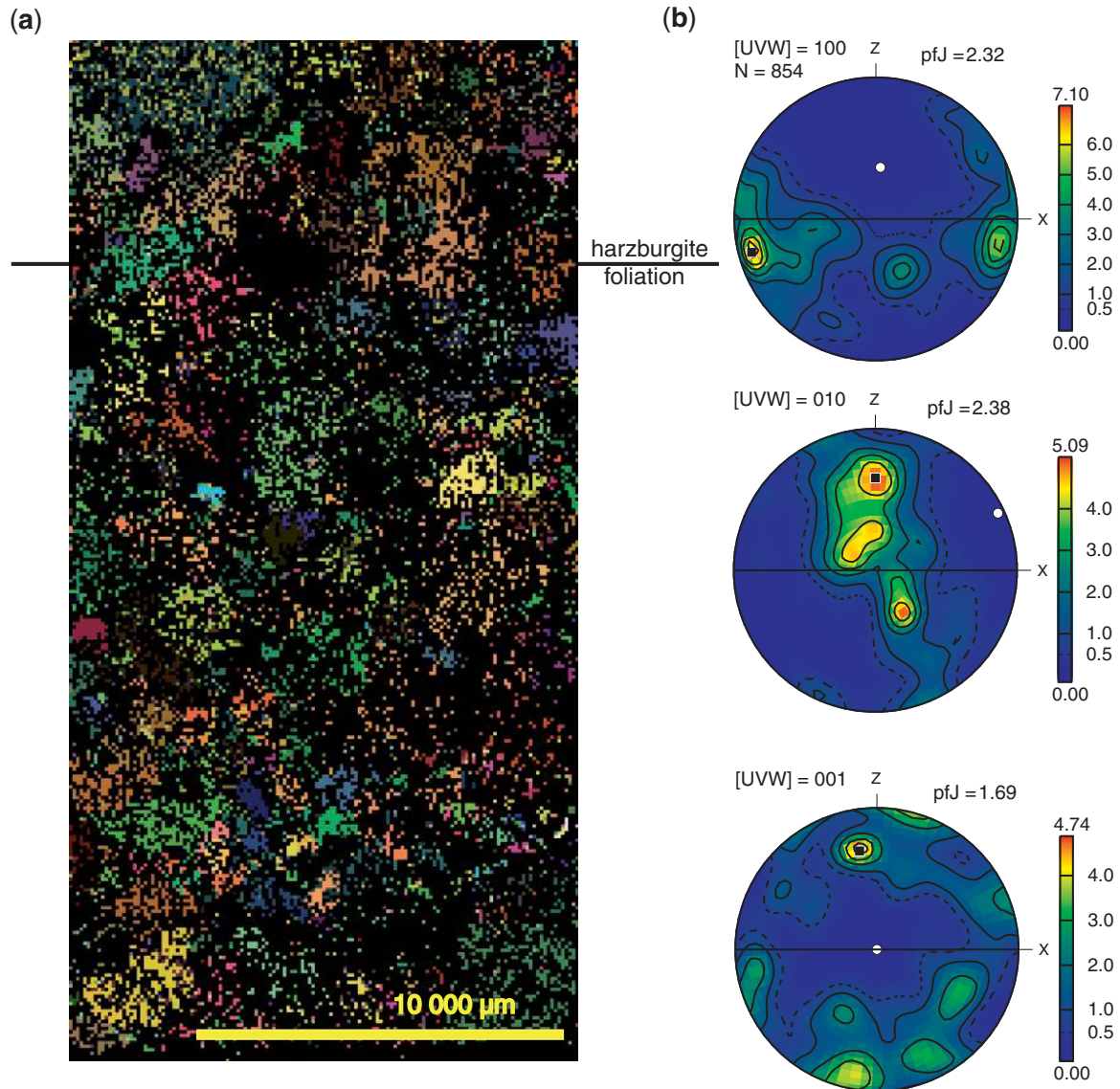
(a)

(b)

Fig. 1. Electron back scattered diffraction (EBSD) map (a) and polar representation of lattice preferred orientation (LPO) (b) of harzburgite sample (97OA129) from the Oman ophiolite. The unfiltered map (a) visualizes the per cent of olivine preserved (the only phase indexed), about 40%. The classical olivine LPO (b), with a maximum of $(010)_{ol}$, high-*T* slip plane at a low angle to the foliation, and $[100]_{ol}$, high-*T* slip line at a low angle to the lineation, is quenched from the suboceanic mantle asthenospheric flow. Lower hemisphere projection; non-polar data; pfJ index representative of the fabric strength after Mainprice & Silver (1993); N indicates number of points per grain.

of this study and was collected 2 km below the petrological Moho in the Oman ophiolite. The serpentinization (60%) has developed pseudomorphic mesh textures, and veins of chrysotile ± magnetite and calcite infiltrate the mesh network. The veins forming the mesh texture (Fig. 2a) have an average thickness of ∼50 μm and a spacing of the order of 200 μm (i.e. no more than one-tenth of the original size of the olivine grains). There is no sharp discontinuity of the mesh networks at olivine grain boundaries. The mesh rims are filled with lizardite pseudofibres that have negative optical elongation (α-serpentine) and are oriented perpendicular to the serpentine rim margin.

Magnetite grains decorate the contact surfaces of adjoining mesh rims of neighbouring altered olivine grains. Orthopyroxene is pseudomorphosed to bastite.

Optical measurements of the orientation of lizardite veins, reported in the peridotite LPO reference system, show that such veins form two populations (Fig. 2b). The first set is parallel to the (010) olivine maximum, and slightly oblique to the foliation. The second set is more diffuse, and its pole forms a girdle in the foliation plane with two submaxima parallel and perpendicular to the lineation, respectively. These geometrical relationships are representative of a common situation for mantle peridotites
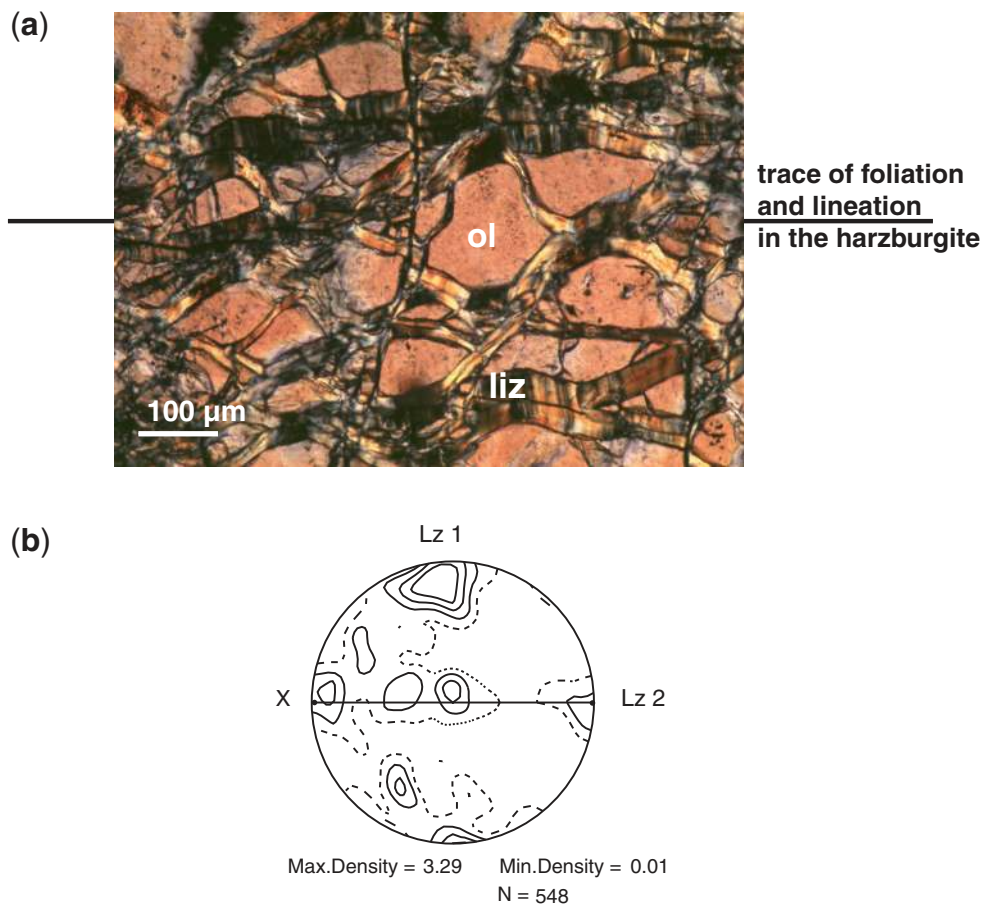
(a)

trace of foliation
and lineation
in the harzburgite

(b)

Fig. 2. (a) Optical microscope, transmitted polarized light image of harzburgite sample 97OAl29. Mesh-textured serpentine is lizardite. Intermesh microveins comprise magnetite. Thin section cut perpendicular to foliation and parallel to lineation in the harzburgite (horizontal is east–west in figure). (b) Poles of lizardite (Lz) veins (548 U-stage measurements, in six thin sections covering the half-space, same reference system as in (a). Lizardite veins are oriented in two sets, subparallel and perpendicular to foliation, respectively (after Dewandel *et al.*, 2003).

from the Oman ophiolite; they are seen in thin sections cut with reference to the peridotite fabric as in Fig. 2a.

Non-topotactic lizardite–forsterite relationships

Our preliminary optical study indicates the best conditions with which to explore the crystallographic relationships between lizardite and its host olivine, using high-resolution, field emission gun scanning electron microscopy (FEGSEM), conventional electron microscopy (CTEM) and selected-area electron diffraction (SAED). From such local examination we address the following question: does the geometrical organization of lizardite mesh networks result from lizardite growth controlled by the crystallography of the host olivine? Knowing the 3D relationships between lizardite and olivine allowed us to select the best contacts in sections perpendicular to the interface of the two phases (Fig. 3a). The TEM and FEGSEM,

low-magnification images of the interface (Fig. 3b and c) show a very sharp contact between olivine and lizardite, without any intermediate mineral phase between them. Diffraction contrast bands in lizardite run normal to the ol–liz interface, and correspond to the serpentine fibres seen optically. At such a small scale, the fibres appear as narrow lizardite crystals assembled in adjoining columns (Fig. 3c). Lizardite cleavage traces (Fig. 3b) mark the (00l) basal planes of lizardite, which lie systematically parallel to the ol–liz interface when close to it. SAED patterns made while selecting several neighbouring lizardite columns at a time confirm that [00l]* lizardite radiates out from the ol–liz contact, and is along the long axis of the lizardite fibres. The analysis of such SAED patterns also indicates that the *a*-axis of 1T-lizardite lies along the ol–liz interface without fixed orientation with respect to the olivine lattice. Thus the set of fibres of columnar lizardite locally forms an axial texture around [00l]$_{liz}$ on
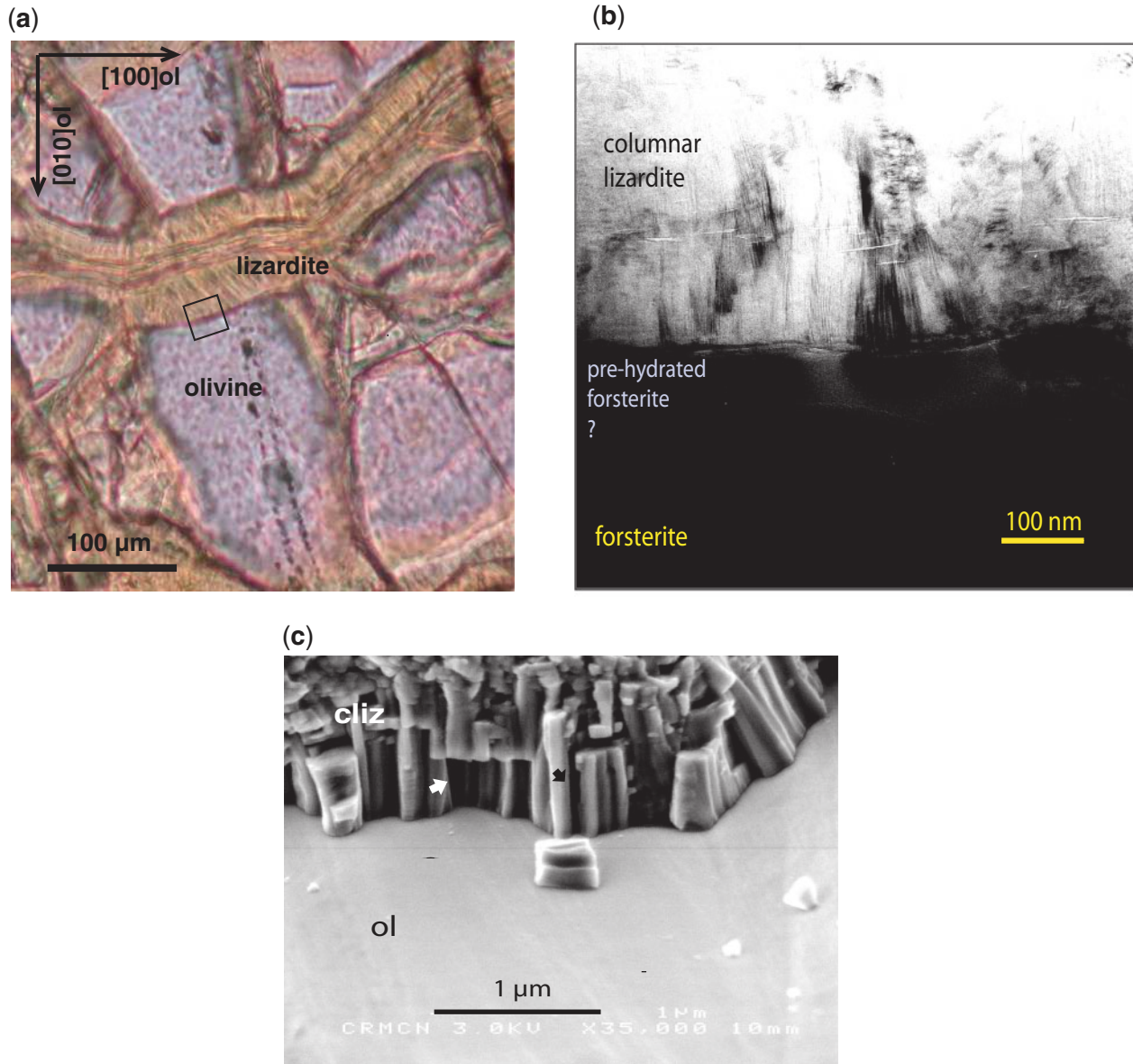
(a)

(b)

(c)

Fig. 3. (a) Lizardite vein observed in the (00l) plane of host olivine, and perpendicular to the vein–olivine interface (optical microscope, transmitted light, parallel Nicols). (b) Low-magnification TEM image of the forsterite–lizardite contact [inset in (a)]. (c) SEM secondary electron image of a broken interface between columnar lizardite (cliz) and olivine (ol). Noteworthy features are the sharp cliz–ol interface, the lateral and vertical disruption of lizardite columns by empty voids (arrows), and the trend of cliz column axes to remain perpendicular to the the local olivine surface (upper right).

olivine surfaces. Accordingly, there are no local topotaxial relationships between olivine and lizardite (Baronnet & Boudier, 200l), only a strong tendency for the lizardite layers to remain parallel to the reacting interface. Integrating this observation over time would indicate that the lizardite basal layer orientation from the rim surface (median line of lizardite veins) to the frozen-in ol–liz interface would follow the shape of the latter from the beginning to the end of the serpentinization process.

Examination of broken surfaces of the Oman sample using high-resolution FEGSEM (Fig. 3c) confirms that the basal lizardite layers are in direct contact with the olivine surface and that lizardite columns 0·1–0·4 μm in width develop normal to the olivine surface on which they sit. Such columns are not continuous over lengths exceeding 1 μm. Instead, many interconnected interstices and microcavities partly isolate lizardite columns from each other and divide the columns along their length.

These are thought to have been pathways for fluid supply in which the fluid exchanged elements to and from the reacting interface during inward growth of lizardite at the expense of the dissolving olivine grain (Baronnet & Boudier, 2001).

ANTIGORITE IN ANTIGORITE SCHIST FROM A DIATREME IN THE COLORADO PLATEAU

The Moses Rock dike, exposed in the central part of the Colorado Plateau, belongs to a series of kimberlitic and lamprophyric diatremes, the 'Navajo Volcanics', with ages of 25–31 Ma. The 6 km long dike comprises a kimberlitic breccia composed of mantle xenoliths and various fragments from the underlying continental crust. The mantle fragments include antigorite schist, jadeite-bearing clinopyroxenite, eclogite, spinel websterite and spinel lherzolite (Smith, 1995), which originated at depths of 50–150 km and temperatures of $\sim$900°C, according to clinopyroxene thermobarometry. Meta-peridotites from these diatremes contain hydrous phases (amphibole, chlorite, clinohumite, antigorite) that indicate hydration conditions of $\sim$600–700°C and 45–60 km.

Optical and fabric measurements

The studied sample MR1 is an antigorite schist, a rare specimen in which the serpentinization ($\sim$60%) preserves the peridotite network (Fig. 4a). A strong foliation is marked by the orientation of antigorite lamellae by the parallel microlayering (millimeter scale) of antigorite–tremolite bands interlayered with primary olivine crystals (Fig. 5a). Primary pyroxenes are totally replaced by amphibole; partly chloritized lobate spinel suggests that the protolith was a spinel peridotite. A few concordant carbonate veins (50 μm thick) crosscut the antigorite–tremolite bands.

Interestingly, in the studied sample, the olivine preserves its primary fabric. This is observed in thin sections cut according to the antigorite fabric (Fig. 5a and b), where olivine crystals show well-restored (100) sub-boundaries, recording a pre-existing asthenospheric mantle flow (Nicolas & Poirier, 1976). In addition, the antigorite lamellae clearly exhibit a dual orientation relative to the host olivine (Fig. 5b), set (1) being parallel to $(100)_{ol}$ sub-boundaries, and set (2) parallel to the $(010)_{ol}$ parting plane. Set (1) is much more frequent, and is responsible for the antigorite schist foliation. This visual orientation is confirmed by olivine CPO measurements (Fig. 4b). The olivine exhibits a strong orthorhombic CPO, characteristic of asthenospheric mantle flow, which would be orthogonal to the antigorite schist fabric. Its projection in the antigorite schist reference system confirms the observed relationships: antigorite main set (1), marking the foliation, is parallel to $(100)_{ol}$, and antigorite set (2) is concordant with the $(010)_{ol}$ plane. The observed crystallographic relationships between olivine and antigorite sets (1) and (2) are explored subsequently by TEM. As noted in the previous section, knowledge of the crystallographic relationships between olivine and serpentine in the studied sample has allowed us to select the best contacts, normal to the olivine–serpentine interfaces, for further study.

Topotactic antigorite–forsterite relationships

Taking advantage of this exceptional sample from Moses Rock, selected contacts between antigorite and its host olivine have been explored using both SEM and TEM, addressing the same type of questions as for lizardite–olivine: what are the crystallographic relationships between the two phases, and what controls antigorite growth in its conditions of stability? The HRTEM image and corresponding microdiffraction pattern on antigorite lamellae (Fig. 6a) exhibit typical features of HT–HP antigorite (Auzende *et al.*, 2002, 2006*a*). The view along $[010]_{atg}$ indicates a very regularly modulated structure, with few defects [no twins, a few modulation dislocations and modulation offsets (stacking faults)], and a unique modulation wavelength of 43·5 Å along the *a*-axis (i.e. $m = 17$, where m is the number of silicate tetrahedra along the wave). The TEM, low-magnification image of the first and most frequent olivine–antigorite interface (Fig. 7) shows an open contact between a $(001)_{atg}$ plane boundary and a $(100)_{ol}$ crenulated boundary. The crenulation marks preferential crystalline resorption along closely spaced $(010)_{ol}$ parting planes. The structure is mainly a two-layer polytype with twice the thickness (2×7.2 Å) of the serpentine layer along c^* (Figs 6a and 8b1) and occasionally a one-layer polytype (Fig. 8b2). In well-localized regions (Fig. 6b), the lattice is affected by numerous kink-bands and stacking faults that mark an early stage of plastic deformation. Rotation of olivine subgrains is marked by the offset or disruption of Bragg fringes at their boundary. SAED patterns and images made on atg–ol junctions (Fig. 8b1 and b2) provide the parameters of the main topotaxy: $[100]_{atg}//$ $[010]_{ol}$; $[010]_{atg}//[001]_{ol}$; and planes in contact as $(001)_{atg}//$ $(100)_{ol}$. The second topotactic association is: $[100]_{atg}//$ $[100]_{ol}$; $[010]_{atg}//[001]_{ol}$; and contact planes as $(001)_{atg}//$ $(010)_{ol}$. These olivine–antigorite relationships correspond to type (1) and (2) contacts observed optically [antigorite lamellae parallel to $(100)_{ol}$ sub-boundaries and to $(010)_{ol}$ parting planes, respectively]. The two types of contacts are seen simultaneously in the low-magnification CTEM image (Fig. 8a), type (1) antigorite lamellae being parallel to the $(100)_{ol}$ often crenulated interface, and type (2) being parallel to the always smooth $(010)_{ol}$ interface. The T-shaped relationships of the two types of antigorite lamellae show that type (1) predates type (2). These relationships suggest that antigorite grew first along planar defects
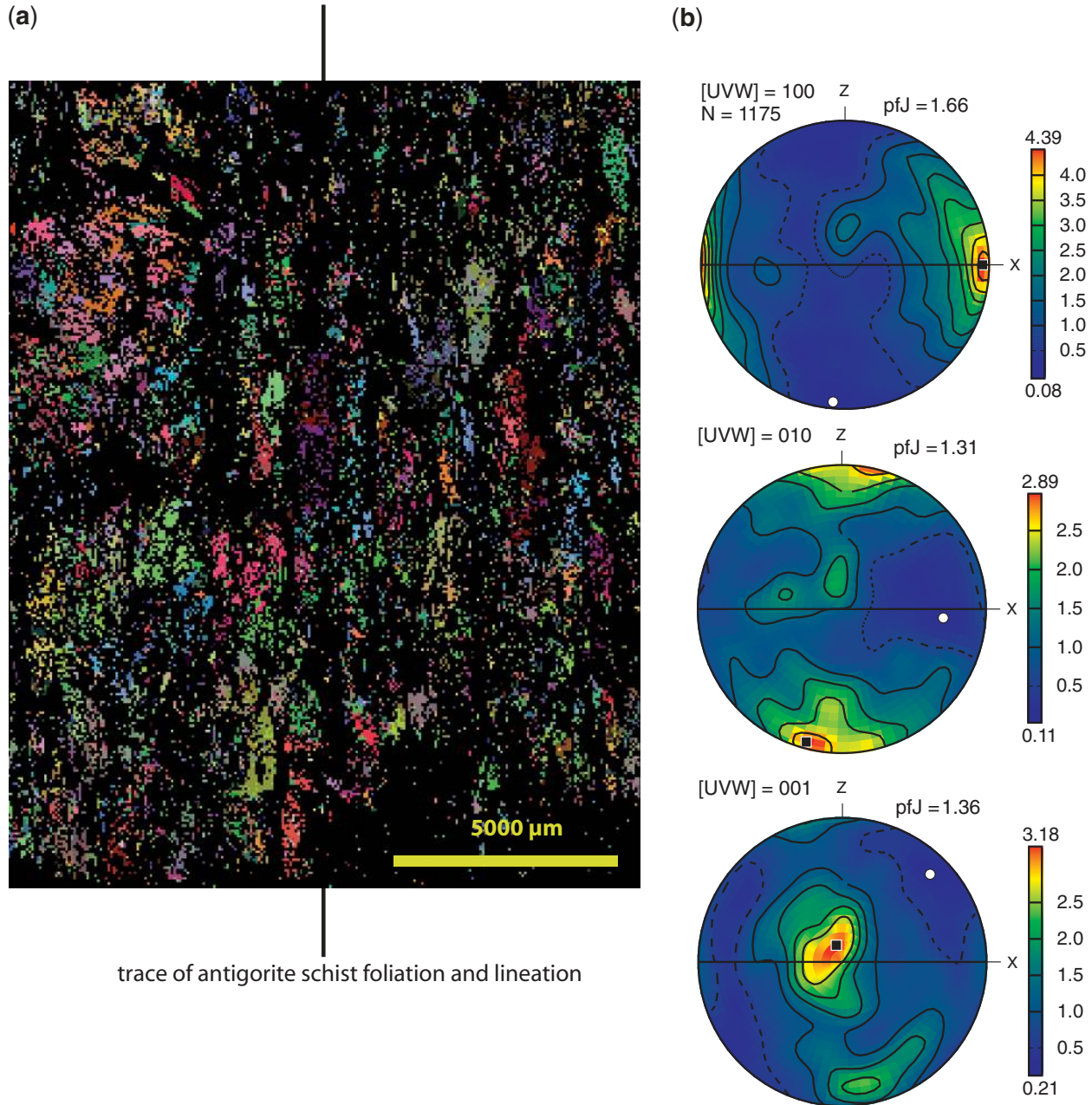
(a)

(b)

trace of antigorite schist foliation and lineation

Fig. 4. Electron back scattered diffraction (EBSD) map (a) and polar representation of lattice preferred orientation (LPO) (b) of olivine in antigorite schist (MR1) from Moses Rock kimberlitic dike on the Colorado Plateau. The unfiltered map (a) visualizes the per cent of olivine preserved (the only phase indexed), about 40%. View in plane perpendicular to foliation, marked by antigorite lamellae (black); host olivine (colored) is interlayered. The olivine LPO (b) is represented in the same antigorite schist reference system as in (a), perpendicular to antigorite foliation (vertical north–south), and parallel to antigorite lineation. Lower hemisphere projection; non-polar data; pfJ index representative of the fabric strength after Mainprice & Silver (1993); N indicates number of points per grain.

propagating along $(100)_{ol}$ as shown in Fig. 9. The TEM image of Fig. 9 visualizes the nucleation of antigorite following a fluid pathway in a 'microcrack' propagating along the $(100)_{ol}$ sub-boundary (or dislocation wall). We assume that dislocation walls $(100)_{ol}$ control the propagation of fluids via a mechanism of plastic mismatch-induced microcracking (Carter & Kirby, 1978). In fact, no defect contrasts were observed ahead of the tip of the antigorite lamellae seen in Fig. 9. However, the line of modulation offset running along the middle of the antigorite lamellae could be inherited from a terminated $(100)_{ol}$ mismatch plane. It is also possible that the field of observation at a
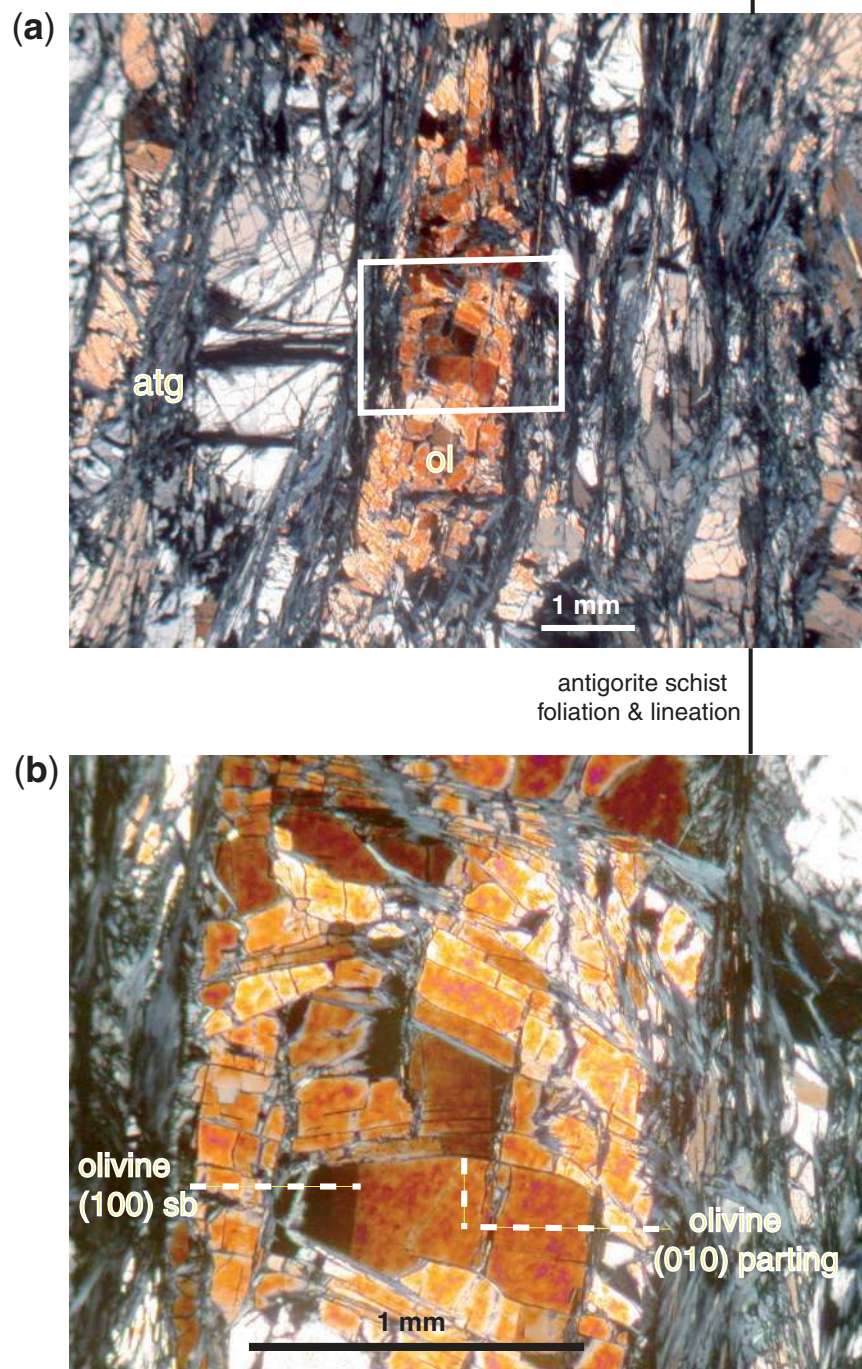
Fig. 5. (a) Optical microscope, transmitted polarized light image of antigorite schist MR1 (same reference orientation as in Fig. 4). (b) Enlargement [area outlined in (a)], showing the dual orientation of antigorite lamellae: antigorite lamellae 1, marking the foliation (vertical in the view plane) parallel to (l00) olivine sub-boundaries, antigorite lamellae 2, parallel to (0l0) olivine parting plane. atg, antigorite; ol, olivine; sb, sub-boundary.
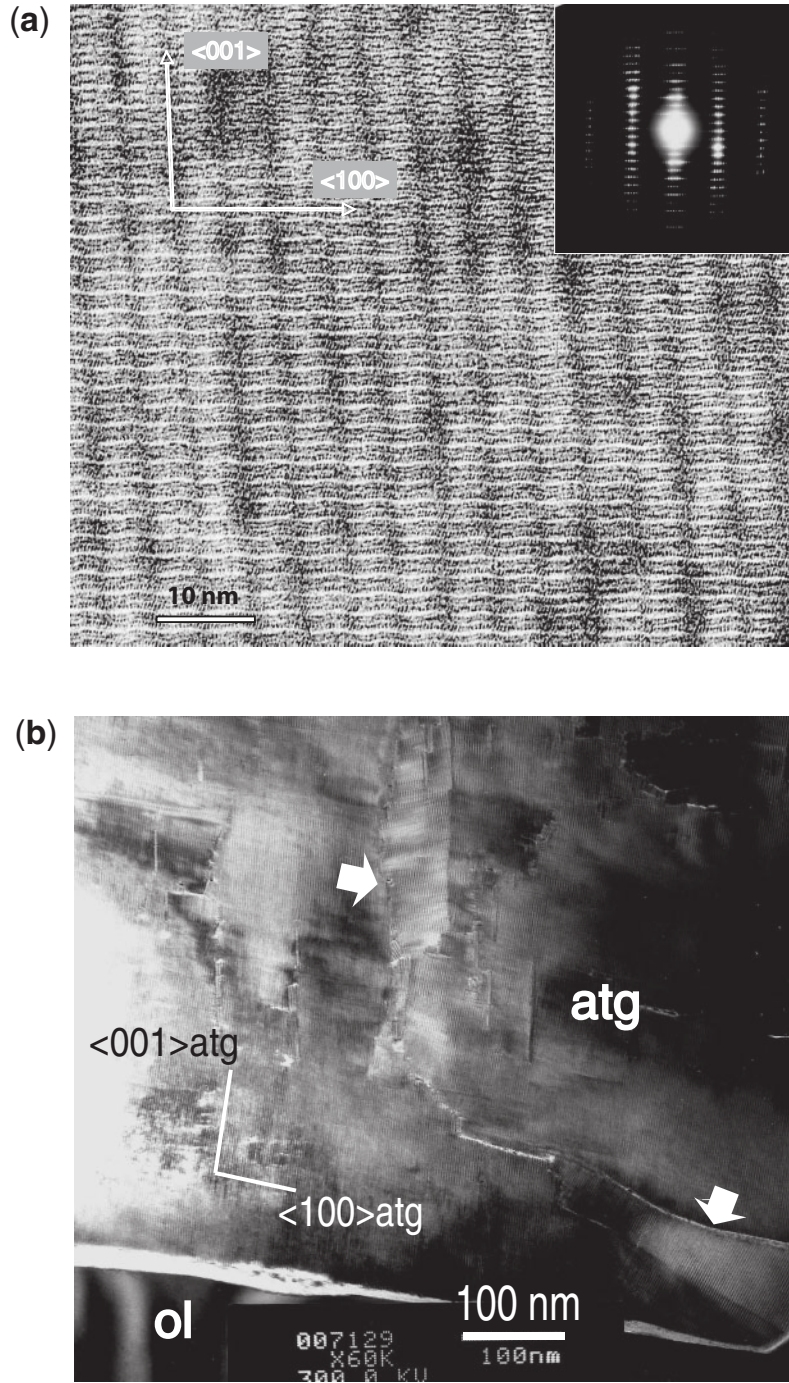
Fig. 6. (a) HRTEM image of an undeformed antigorite region viewed along [0l0], and corresponding microdiffraction pattern (inset). Very regular modulation wavelength of 43·5 Å, with a few defects. Two-layer polytypic structure with double period along c^* ($2 \times 7 \cdot 2\,\text{Å} = 14 \cdot 4\,\text{Å}$). The above features are indicative of HT–HP antigorite. (b) Low-magnification, bright-field CTEM image of defective antigorite (atg) in contact with olivine (ol). Subvertical stripes in atg are (l00) modulation lattice fringes. Kink-bands (arrows) mark local plastic deformation of the antigorite structure.
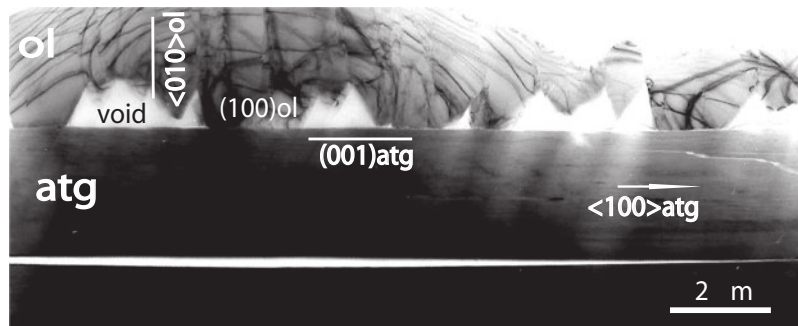
Fig. 7. Open contact of well-developed antigorite (atg) against forsteritic olivine (fo). The basal face $(001)_{atg}$ is parallel to $(100)_{ol}$ crenulated boundary. Triangular voids each point to closely spaced traces of $(0l0)_{ol}$ partings. They indicate preferential olivine resorption there, and they make presumably ultimate pathways for access of the hydrating fluid to the reaction interface.

scale of 100 nm is below the dimension of edge dislocation spacing $(0{\cdot}1{-}1\,\mu m)$ in well-restored olivine crystals (Gueguen, 1979). The second plane of topotactic growth of antigorite $(0l0)_{ol}$ is the slip plane of HT plastic flow in olivine, which is also the most probable de-cohesion plane, the only dense plane for which Si–O bonds are not broken during slip or cracking (Nicolas & Poirier, 1976).

Figure 10 schematically illustrates the observed crystallographic relationships between olivine and antigorite sets (1) and (2) as they are deduced from optical and electron microscopy.

DISCUSSION
Ocean-floor serpentinization

Lizardite, the penetrative mesh serpentine, which is developed under static conditions, is the dominant form of serpentine in the shallow ocean mantle (O'Hanley, 1996; Mével, 2003). The geometrical relationship of the lizardite network with the internal structure of the peridotite mineral aggregate is such that the lizardite veins are statistically parallel or perpendicular to $(0l0)_{ol}$, as shown by Dewandel *et al.* (2003) and in Fig. 2. This is probably the common situation in peridotites from the oceanic lithosphere, at least in fast-spreading systems as recorded by the Oman and other ophiolites. This inference is based on generalized observations in thin sections cut in the appropriate *xz* structural plane of the olivine aggregate. The α-serpentine filling the mesh is columnar lizardite with $(00l)_{liz}$ parallel to the margin of the vein and in nontopotactic contact with the host olivine, as illustrated in the present study. The consequence is that, as lizardite growth is not directly controlled by the crystallography of olivine, it has to be controlled by the geometry of the vein network; that is, by the geometry of the cracking system. Thus the mesh framework images the initial cracks through which hydrous fluids penetrated the peridotite aggregate, inducing lizardite nucleation and growth from the crack towards the centre of the host olivine grains.

The cracking is stress-induced when the peridotite shifts from the ductile to the brittle regime during cooling, at a lithostatic pressure of about 100–200 MPa.

Boudier *et al.* (2005) proposed that the measured geometrical relationships that link the lizardite mesh framework with the anisotropy of the peridotite aggregate should be assigned to the anisotropy of thermal contraction during cooling. In support of this hypothesis is the finding that forsteritic olivine has a strong thermal anisotropy, such that $[0l0]_{ol}$ is the axis of maximum thermal contraction (Bouhifd *et al.*, 1996). As deduced from the peridotite fabric in the shallow oceanic mantle, the $(0l0)_{ol}$ plane coincides with the high-T mantle flow plane, and the spreading geometry recorded by the mantle flow-related foliation is horizontal (Fig. 11). Applying the experimental data of Bouhifd's on thermal expansion of forsterite to a network having the geometry of mesh lizardite ($\sim$200 μm mesh-size) would produce 1 μm wide microcracks during cooling from 800°C to 400°C. This thermally induced microcracking network would generate an oriented porosity ($\sim$0·01 %) driving seawater horizontally, and would initiate the development of lizardite along $(0l0)_{ol}$, when reaching its temperature of stability. Subsequently, the serpentinization would progress inward toward the mesh cores of olivine crystals as the water/rock ratio increases.

Serpentinization of the mantle wedge above a subducted slab

Tremolite–antigorite schists are the most common type of ultramafic rock inclusion in the Moses Rock 'kimberlitoid' diatreme, among a suite of xenoliths that includes websterites, eclogites and peridotites that are inferred to have sampled the mantle wedge above the subducting Farallon plate. The xenolith suite is affected by a retrograde hydrous metamorphism that has been assigned to a shallowing of the subducted slab during the Laramide episode, at 80 Ma (Dumitru *et al.*, 1991; Helmstaedt & Schulze, 1991; Humphreys & Coblentz, 2007). These retrograde reactions
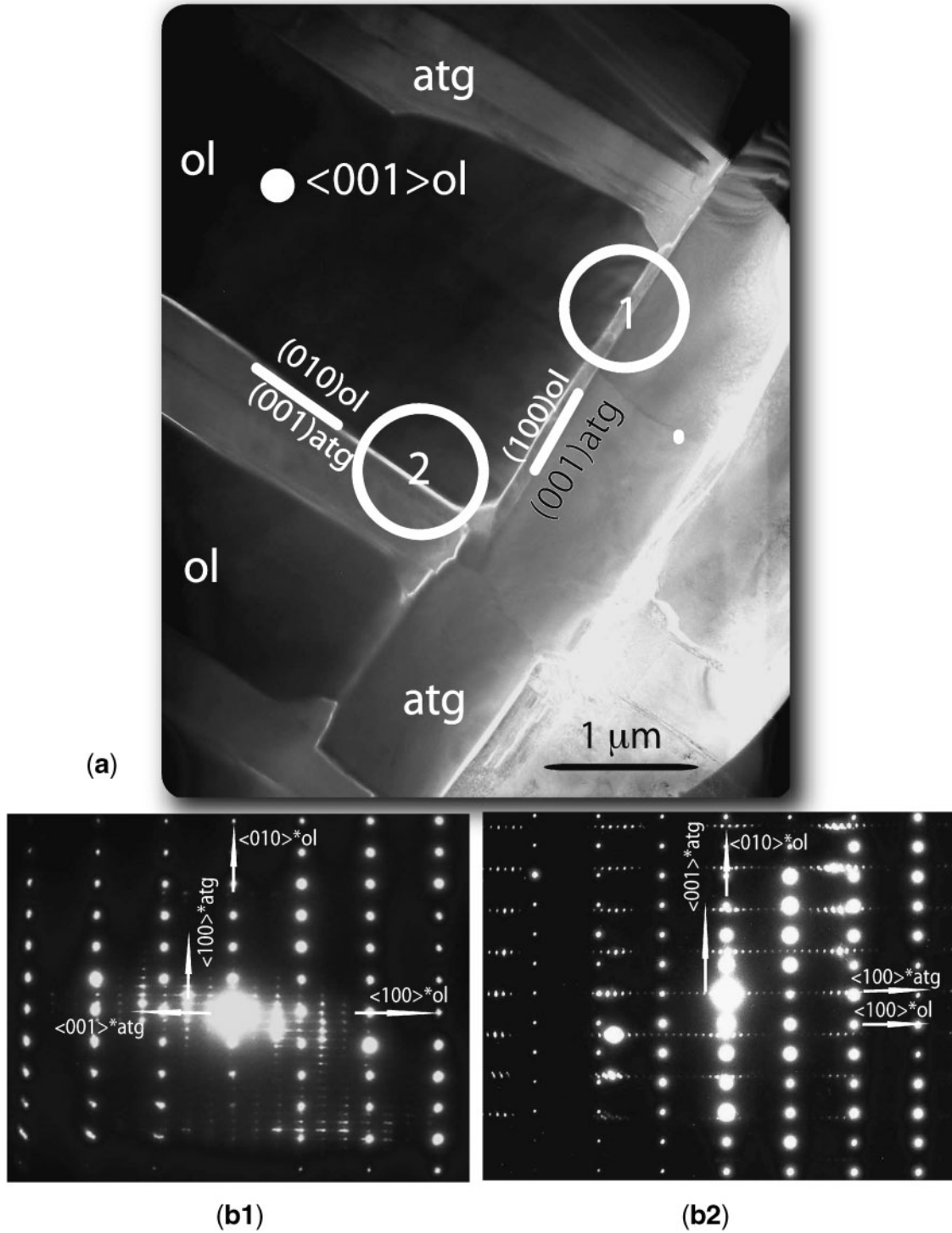
Fig. 8. CTEM data on olivine–antigorite contacts. (a) Low-magnification, bright-field image of the two types of orientation of antigorite lamellae in olivine host, (1) parallel to $(100)_{ol}$, often a crenulated contact, and (2) parallel to $(010)_{ol}$, as a smooth contact. (b1, b2) Electron diffraction patterns of regions corresponding to circled areas in Fig. 8a. $[u\ v\ w]_{ol,atg}$* refers to reciprocal directions. It should be noted that $[100]_{atg}$* is $1-2°$ ($\beta_{atg} - \Pi/2 = 16°$) off $[010]_{ol}$*: this is best seen looking at (b2) under grazing incidence from right to left. In both cases the zeroth-order Laue zones of the $hk0_{ol}$ and $h0l_{atg}$ diffraction nets are not strictly coincident. From these data, the approximate atg–ol topotaxial relationships are: (b1): $[100]_{atg}//[010]_{ol}$; $[010]_{atg}//[001]_{ol}$; (b2): $[100]_{atg}//[100]_{ol}$; $[010]_{atg}//[001]_{ol}$.
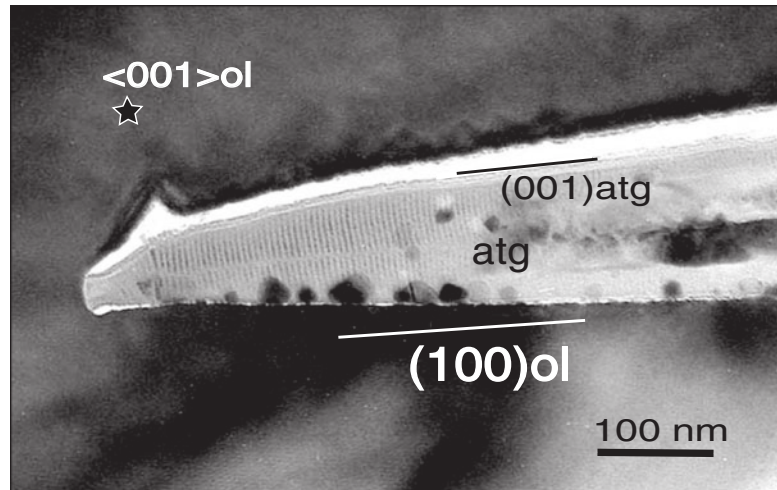
Fig. 9. CTEM, bright-field image of the termination of an antigorite lamella tip grown parallel to $(100)_{ol}$, and showing the crenulated olivine margin on both sides of the 'microcrack'. The median line inside antigorite separates two trains of modulation fringes in offset positioning. Such an antigorite defect, ending at the lamella tip, is presumably inherited from a 'past' (100)ol planar defect. The white edge corresponds to a void presumably occupied by a fluid film. Tiny crystals on the tight atg–ol boundary are artifacts (sputtering of Cu from the TEM grid during ion milling).
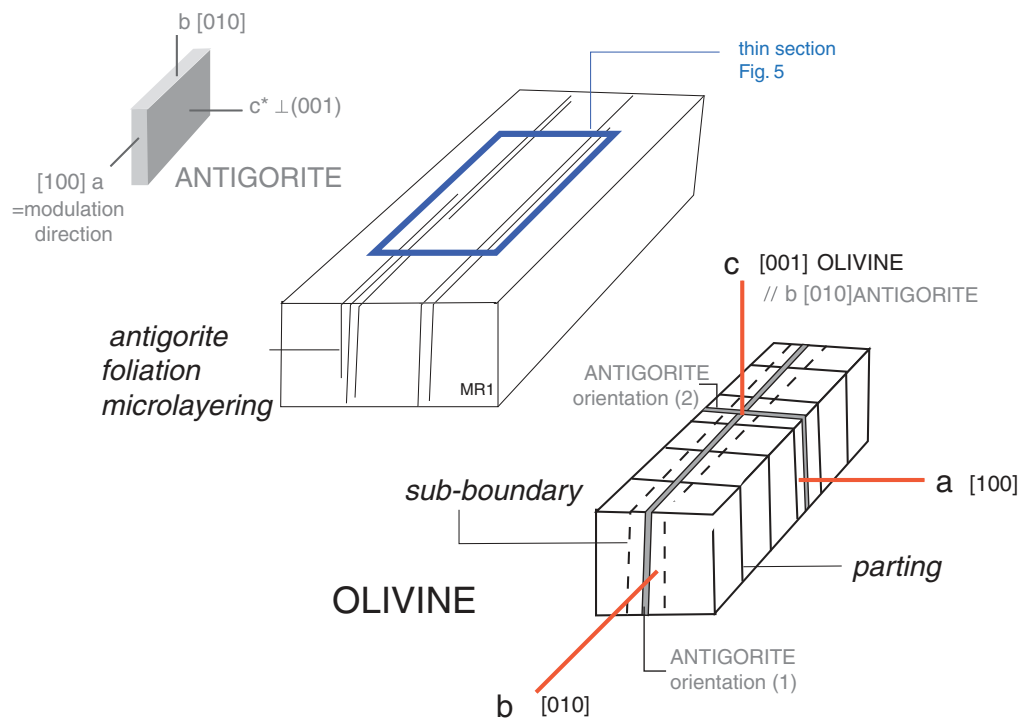

Fig. 10. A 3D visualization of olivine–antigorite crystallographic relationships in antigorite schist MR1 as observed in thin section of Fig. 5, with orientation (1) and (2) of antigorite lamellae deduced from optical and electron microscope studies. $b[010]_{atg}$ is parallel to $c[001]_{ol}$ in both relationships.

are thought to have taken place in the subcontinental upper mantle at pressures up to 2·2 GPa and temperatures of 500–700°C (Smith, 1979; Roden *et al.*, 1990). According to Smith (1995), the hydration may have been restricted to shear zones that traversed the lower crust and lithospheric mantle to at least 75 km depth.

The studied sample (MR1) is highly unusual in that 40% of the primary olivine is preserved, allowing
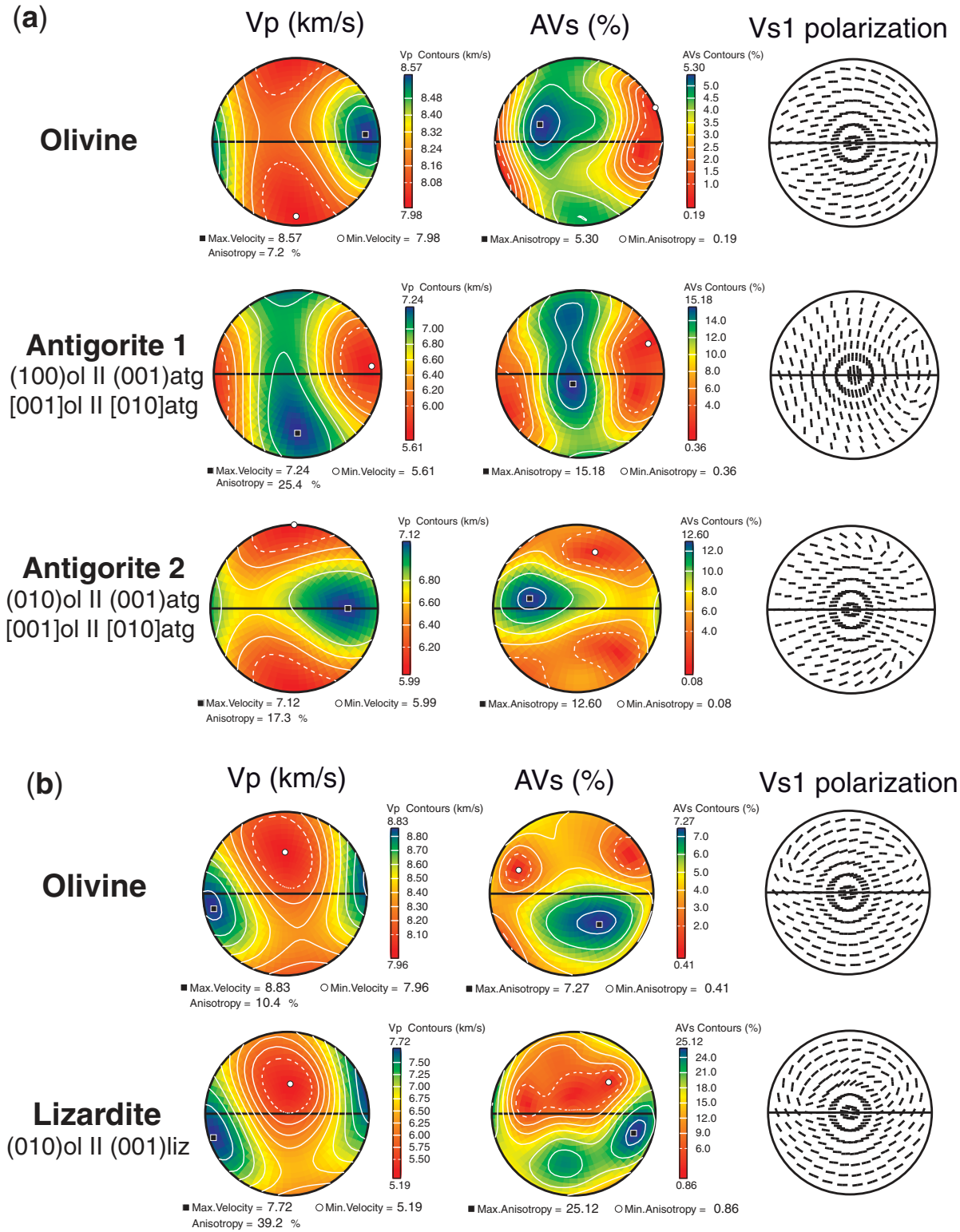
Fig. 11. Pole figures of P- and S-wave distribution for antigorite and lizardite pure polycrystalline aggregate computed from olivine CPO and the topotaxy relations (for details, see Electronic Appendix). (a) Pole figure for olivine and antigorite, calculated from olivine CPO in sample MR1 (Fig. 4b) and antigorite 1 and 2 relationship to olivine. (b) Pole figure for olivine and lizardite, calculated from olivine CPO in sample 97OAl29 (Fig. 1b) and lizardite relationship to olivine.

observation of its textural relationships with the secondary hydrous phase. Our study has shown that the HP–HT antigorite is in two topotaxial relationships with olivine, and that the basal plane $(001)_{atg}$ lies in contact with interfaces $(100)_{ol}$ or $(010)_{ol}$. The other very interesting and surprising result of this study is that a fluid pathway has been identified as open voids along the $(100)_{ol}$ interface boundary, suggesting that a circulating fluid has controlled antigorite nucleation, as in the case of lizardite growth. However, conversely, our TEM images suggest that antigorite nucleated on deformation-induced planar defects in olivine, and that antigorite nucleation followed shortly after the deformation event. It is likely that fluid pressure was competing with lithostatic pressure. Accordingly, olivine microcracking could have been fluid-induced. If so, such an aqueous fluid phase could have infiltrated the peridotite, as suggested by the vein geometry in our images, and would have progressed along specific planes in the olivine crystal; that is, $(100)_{ol}$ dislocation walls and $(010)_{ol}$ HT slip planes (or parting planes). We infer that $(100)_{ol}$, which is the locus of edge dislocation piling (Nicolas & Poirier, 1976), potentially channels the entry of water. The $(010)_{ol}$ plane is the preferred cleavage plane, having the minimum fracture surface energy, both calculated and measured (Swain & Atkinson, 1978; Atkinson & Meredith, 1987). The implication of our data would be to assign the non-topotaxial relationships characterizing lizardite versus the topotaxial growth of antigorite to the documented dissimilar cracking modes. Lizardite would develop in pre-existing microcracks along loose olivine interfaces corroded by fluid circulation, whereas antigorite would nucleate via instantaneous hydration along tight dislocation walls.

These data provide some constraints on fluid circulation when transposed to the scale of the anisotropic peridotite aggregate lying at depth in the mantle wedge. First, the preservation of the olivine aggregate with its high-T mantle flow texture and CPO in the MR1 antigorite schist indicates that the antigorite developed after cooling of the mantle wedge at lithospheric temperatures. Seismic anisotropy in the mantle underneath the Colorado Plateau, as in other suprasubduction-zone mantle wedges, suggests that the asthenospheric mantle has a horizontal flow direction (NNW below the Colorado Plateau; Richardson, 1992). This geometry would correspond to an olivine CPO such that $(010)_{ol}$ is horizontal statistically, and $(100)_{ol}$ vertical and normal to the mantle flow direction. Thus the slab dehydration-induced fluid circulation in the mantle wedge would be, as inferred from our data, controlled first by vertically oriented $(100)_{ol}$ dislocation walls controlling vertical cracking, and then by horizontally oriented $(010)_{ol}$ decoupling planes.

Seismic modelling

The consistent olivine–serpentine relationships documented here suggest that the seismic properties of hydrated mantle could be inherited from these as a result of the olivine CPO in mantle peridotite. Thus we propose a model for the seismic properties of hydrated peridotite that is applicable to the general situation of oceanic lithospheric mantle. We calculated first the CPO of pure polycrystalline aggregates of lizardite and antigorite, using the CPO of olivine measured by EBSD from samples MR1 and 97OA129 (Figs 4b and 1b, respectively) and the topotactic relations given above for serpentine (Mainprice et al., 1990) (further details are given in the Electronic Appendix, available for downloading at http://www.petrology.oxfordjournals.org). Using the elastic constants of single crystals of olivine, lizardite and antigorite as reported by Abramson et al. (1997), Auzende et al. (2006a, b) and Mainprice & Pellenq (personal communication), we have calculated the seismic properties of end-member olivine, antigorite and lizardite. These are represented (Fig. 11) as pole figures, in lower hemisphere projections, of the compressional wave velocity (V_p), shear-wave splitting anisotropy (AV_s) and the polarization of the fastest S wave (V_{s1}). Both olivine CPOs (MR1 and 97OA129) are typical of upper mantle olivine CPO (Ben Ismaïl & Mainprice, 1998) with high P-wave velocity (V_p) parallel to the lineation, high shear-wave splitting in the foliation plane normal to the lineation, and the polarization of the fastest S wave parallel to the foliation. The anisotropy of V_p (7·2–10·2%) and shear-wave anisotropy (5·3–7·3%) is typical for a pure olivine aggregate. The antigorite 1 $(100)_{ol}//(001)_{atg}$ relation (Fig. 11a) results in a radical change in the anisotropy pattern, with the V_p maximum normal to the olivine foliation plane; the high shear-wave splitting is in the same position as olivine in the foliation plane normal to the lineation, but the polarization of the fastest S wave is now normal to the olivine foliation plane. The antigorite 2 $(010)_{ol}//(001)_{atg}$ relation (Fig. 11a) results in a minor change in the anisotropy pattern, with the V_p maximum close to the olivine lineation, the high shear-wave splitting in the olivine foliation plane at an intermediate position between the lineation and its normal, but the polarization of the fastest S wave parallel to the olivine foliation plane. The lizardite $(010)_{ol}//(001)_{liz}$ relation (Fig. 11b) results in a similar pattern to olivine. The major change is the increase in magnitude of the anisotropy of the serpentine aggregates, V_p (25·4, 17·3, 39·2%) and V_s (15·2, 12·6, 25·1%) for antigorite relations 1, 2 and lizardite, respectively.

We then calculated the seismic anisotropy of the olivine + antigorite and olivine + lizardite aggregate as a function of volume fraction using differential effective medium (DEM) modelling (e.g. Mainprice, 1997). As the antigorite $(100)_{ol}//(001)_{atg}$ relation is more frequent we have used this and the lizardite $(010)_{ol}//(001)_{atg}$ relation in Fig. 12. The comparison of the seismic anisotropy of olivine with antigorite and lizardite as a function of volume fraction illustrates the strong differences between the topotaxy of the
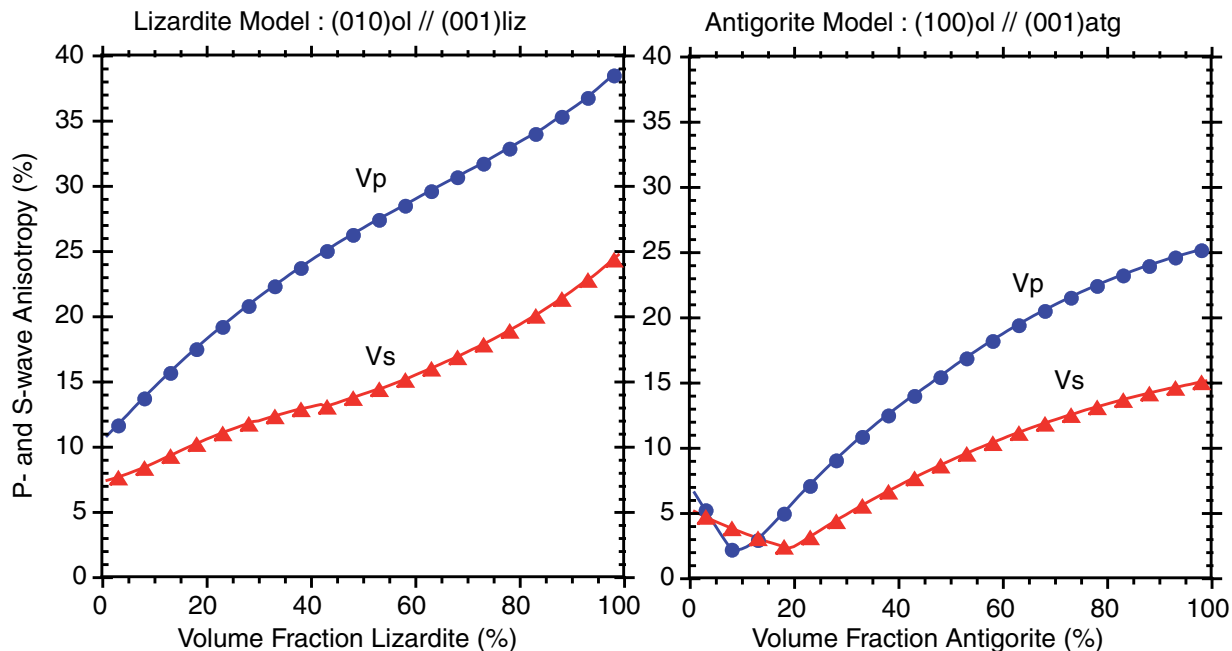
Fig. 12. Calculated seismic anisotropy of the olivine + lizardite and the olivine + antigorite aggregate as a function of volume fraction. The lizardite model $(010)_{ol}//(001)_{liz}$ results in a constructive interference of the seismic anisotropy. The antigorite model corresponding to the dominant relationship $(100)_{ol}//(001)_{atg}$ results in a destructive interference for low degree of serpentinization, then in increasing anisotropy with serpentinization increase.

two forms of serpentine. At very low volume fractions of serpentine, there is the influence of the initial olivine CPO, with antigorite-bearing sample MR1 having a weaker CPO and seismic anisotropy than the lizardite-bearing sample 97OA129 (Figs 4b and 1b, respectively). However, the most important difference is the constructive nature of lizardite anisotropy with that of olivine, whereas the effect of antigorite is destructive, resulting in a low anisotropy below 20% transformation. Above 20% volume fraction antigorite the anisotropy steadily increases, but the orientation of this anisotropy is very different from that of the original olivine.

The two different scenarios for serpentinization of olivine are shown schematically in Fig. 13. In the mantle wedge and downgoing plate antigorite is expected to be the stable serpentine mineral, whereas on the ocean floor and at shallow depths in the oceanic lithosphere lizardite is the common form. In the mantle wedge below an island arc (e.g. NE Japan) a typical olivine [100](010) CPO (A-type like MR1 or 97OA129) for horizontal asthenospheric mantle flow towards or away from the trench would produce trench-normal fast S-wave polarization anisotropy for vertically propagating waves. In contrast, the olivine [100](010) CPO for a sample hydrated to antigorite would produce initially an almost isotropic seismic signal at volume fractions of less than 20% of antigorite and a trench-parallel fast S-wave polarization at higher

volume fractions. In the downgoing plate the scenario would be identical, and geometrically similar to the outer-rise fault model recently proposed by Faccenda *et al.* (2008) for trench-parallel anisotropy. It is interesting to speculate that the formation of antigorite could facilitate the initiation or preservation of such fault systems at depth, given the topotaxy with olivine. The presence of lizardite in the ocean floor will not be detected by a change in the orientation of the anisotropy, but rather by the increased magnitude with increasing degree of serpentinization. This conclusion is restricted to fast-spreading ocean floor as documented here.

CONCLUSIONS

Based on factual evidence that serpentine growth has an orientation consistent with the crystal lattice of the host olivine, we have explored the serpentine–olivine interface at a sub-micron resolution scale and acquired related crystallographic data for two peridotites that are moderately serpentinized, preserving up to 40% of the host olivine. The serpentine minerals studied, lizardite and antigorite, have contrasting crystallographic relationships with their host olivine. TEM images of the olivine–serpentine interface show that mesh-textured serpentine in harzburgite (97OA129) from the Oman ophiolite is composed of columnar lizardite, forming pseudo-fibres observed by optical
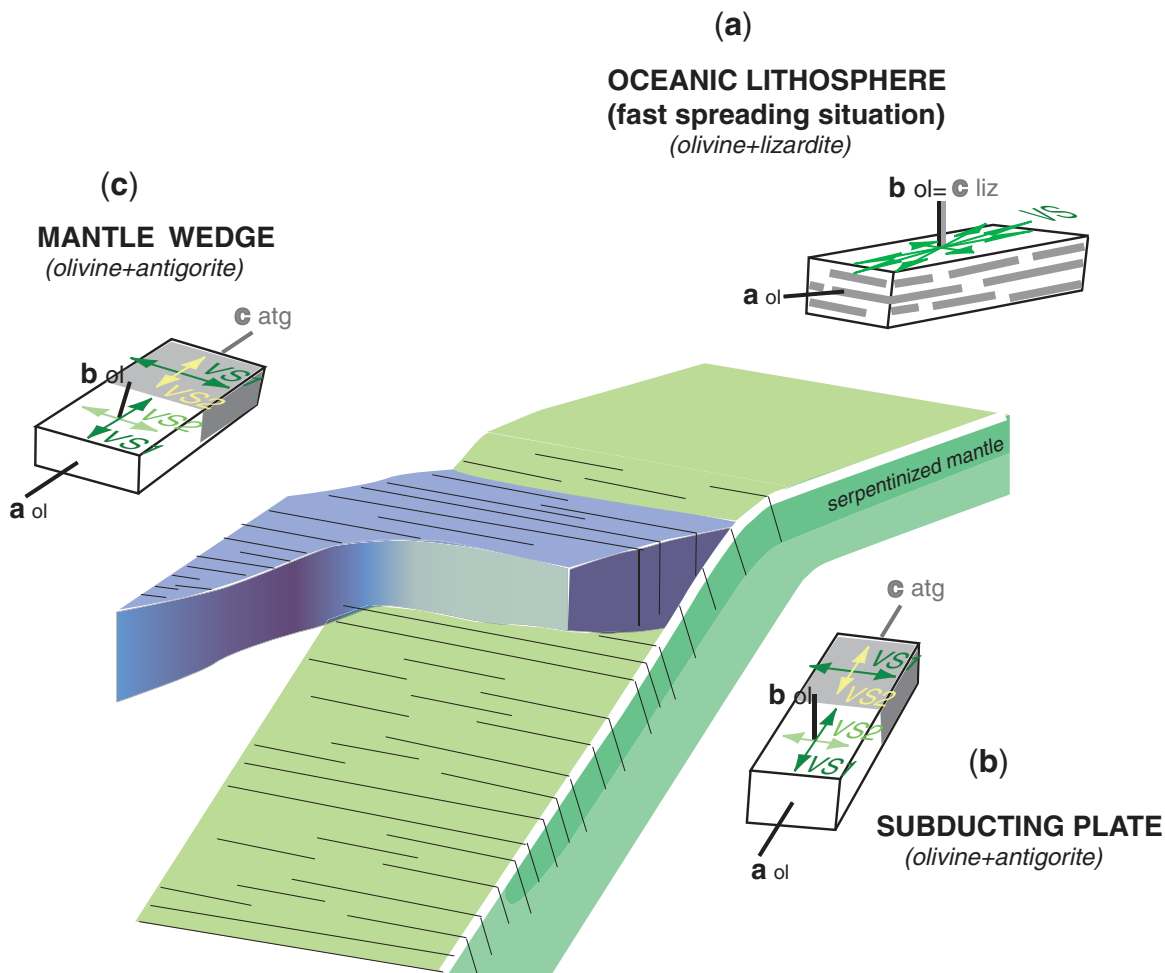
Fig. 13. Restoration, at the geodynamic scale, of geometrical relationships between olivine–serpentine and inferred seismic splitting behaviour. (a) Ocean-floor serpentinization at shallow level. The shallow mantle originating at fast-spreading ridges has a flat foliation, and the flow direction ($[100]_{max}$ of olivine) is parallel to P-wave maximum and to fast S wave. The present study suggests that the dominant lizardite veining is flat-lying, induced by horizontal cracking. Increasing lizardite development results in increasing the anisotropy, but obliterating the orientation of S-wave polarization. (b) Subducting plate. Serpentinization in the hydrated mantle of a subducting plate reaching the domain of antigorite stability would produce initially an almost isotropic seismic signal at low volume fractions of antigorite and then a trench-parallel fast S-wave polarization at higher volume fractions. (c) Mantle wedge. If peridotite foliation in the mantle wedge is horizontal, the development of antigorite resulting from slab dehydration would produce an isotropic signal for low degree of serpentinization, and fast S-wave polarization perpendicular to the fossilized spreading direction for increasing serpentinization.

microscopy (crossed polars). The base of the $(00l)_{liz}$ columns parallel $(0l0)_{ol}$ and are in non-topotactic contact with the olivine surface, in agreement with Rumori *et al.* (2004). SEM images show that columnar lizardite grows inwards at the expense of host olivine from a pre-existing microcrack network inferred to be thermally induced.

Antigorite in an antigorite schist from Moses Rock, a kimberlite-hosted xenolith from the Colorado Plateau, exhibits a dominant orientation with its foliation parallel to an antigorite–olivine microlayering. The antigorite lamellae are parallel to $(100)_{ol}$ sub-boundaries (or dislocation walls). From this orientation, they develop the antigorite schist foliation that is normal to the original peridotite high-T foliation. A subsidiary orientation of antigorite lamellae is parallel to the $(0l0)_{ol}$ parting. TEM imaging documents the topotactic relationship between antigorite and its host olivine along an interface $(001)_{atg}/(100)_{ol}$, such that the antigorite modulation ($43{\cdot}5\,\text{Å}$) along $[100]_{atg}$ corresponds roughly to four times the $[100]_{ol}$ parameter. TEM imaging has allowed access to the very initiation of antigorite growth, showing that antigorite nucleated at the tip of a microcrack propagating along the $(100)_{ol}$ plane. It is inferred that antigorite nucleation is controlled by fluid-invaded crystal defects, and that fluid migration and antigorite nucleation are coeval.

In both cases, the geometrical parameter controlling the orientation of the serpentine is the anisotropy of the original olivine aggregate. Because most mantle peridotites have a marked preferred orientation of olivine crystals inherited from asthenospheric mantle flow, serpentine aggregates must have a preferred orientation inherited from the host olivine anisotropy that we have explored here. Having explored the seismic implications of these consistent relationships, we suggest that anisotropy of propagation of seismic waves as a result of olivine fabric is maintained and reinforced because of the development of lizardite in the hydrated lithospheric mantle of the ocean basins, at least for conditions of fast spreading. Conversely, the development of antigorite in the hydrated mantle of a subducting plate or in the overlying mantle wedge produces a trench-parallel fast S-wave polarization and an anisotropy that is reduced at low degrees of serpentinization but then increases with increasing serpentinization.

ACKNOWLEDGEMENTS

SUPPLEMENTARY DATA

Supplementary data for this paper are available at *Journal of Petrology* online.

REFERENCES

Abramson, E. H., Brown, J. M., Slutsky, L. J. & Zang, J. (1997). The elastic constants of San Carlos olivine to 17 GPa. *Journal of Geophysical Research* **102**, 12253–12263.

Atkinson, B. K. & Meredith, P. G. (1987). Experimental fracture mechanics data for rocks and minerals. In: Atkinson, B. K. (ed.) *Fracture Mechanics of Rocks*. New York: Academic Press, pp. 477–519.

Auzende, A.-L., Devouard, B., Guillot, S., Daniel, I., Baronnet, A. & Lardeaux, J. M. (2002). Serpentinites from Central Cuba: petrology and HRTEM study. *European Journal of Mineralogy* **14**, 905–914.

Auzende, A.-L., Guillot, S., Devouard, B. & Baronnet, A. (2006*a*). Behaviour of serpentinites in convergent context: Microstructural evidence. *European Journal of Mineralogy* **18**, 21–33.

Auzende, A.-L., Pellenq, R. J.-M., Devouard, B., Baronnet, A. & Grauby, O. (2006*b*). Atomistic calculations of structural and elastic properties of serpentine minerals: the case of lizardite. *Physics and Chemistry of Minerals* **33**, 266–275, doi:101007/s00269-006-0078-x.

Baronnet, A. & Boudier, F. (2001). Microstructural and microchemical aspects of serpentinization. In: *Eleventh Annual V. M. Goldschmidt Conference, Hot Springs, VA*, Session 46: Crystal Structures and Mineral Behaviour, Abstract 3382.

Ben Ismaïl, W. & Mainprice, D. (1998). An olivine fabric database: an overview of upper mantle fabrics and seismic anisotropy. *Tectonophysics* **296**, 145–157.

Boudier, F., Nicolas, A. & Mainprice, D. (2005). Does anisotropy of thermal contraction control hydrothermal circulation at the Moho level below fast spreading oceanic ridges? *International Geology Review* **47**, 101–112.

Bouhifd, M. A., Andrault, D., Fiquet, G. & Richet, P. (1996). Thermal expansion of forsterite up to the melting point. *Journal of Geophysical Research* **23**, 1143–1146.

Carter, N. & Kirby, S. (1978). Transient creep and semibrittle behavior of crystalline rocks. *Pure and Applied Geophysics* **116**(4–5), 807–839.

Christensen, N. (1966). Elasticity of ultrabasic rocks. *Journal of Geophysical Reasearch* **71**, 5921–5931.

Dewandel, B., Boudier, F., Kern, H., Warsi, W. & Mainprice, D. (2003). Seismic wave velocity and anisotropy of serpentinized peridotite in the Oman ophiolite. *Tectonophysics* **370**, 77–94.

Dumitru, T. A., Gans, P. B. & Miller, E. L. (1991). Refrigeration of the western Cordilleran lithosphere during Laramide shallow-angle subduction. *Geology* **19**, 1145–1148.

Faccenda, M., Burlini, L. & Mainprice, D. (2008). Fault-induced seismic anisotropy by hydration in subducting oceanic plates. *Nature* **455**, 1097–1100.

Gillis, K., Mével, C., Allan, J. *et al.* (1993). *Proceedings of the Ocean Drilling Program, Initial Reports* **147**, College Station, TX: Ocean Drilling Program.

Gueguen, Y. (1979). Dislocations in naturally deformed terrestrial olivine: classification, interpretation, implications. *Bulletin of Mineralogy* **102**, 178–183.

Helmstaedt, H. H. & Schulze, D. J. (1991). Early to Mid-Tertiary inverted metamorphic gradient under the Colorado Plateau: evidence from eclogite xenoliths in ultramafic microbreccias, Navajo Volcanic Field. *Journal of Geophysical Research* **96**, 13225–13235.

Humphreys, E. & Coblentz, D. (2007). North America dynamics. *Reviews of Geophysics* **45**, 1–30.

Iturrino, G. J. & Christensen, N. I. (1990). Seismic velocities and elastic properties of oceanic gabbros recovered from site 735. In: Mével, C., Gillis, K. M., Allan, J. F. & Meyer, P. S. (eds) *Proceedings of the Ocean Drilling Program, Scientific Results, 118*. College Station, TX: Ocean Drilling Program, pp. 227–244.

Mainprice, D. (1997). Modelling anisotropic seismic properties of partially molten rocks found at mid-ocean ridges. *Tectonophysics* **279**, 161–179.

Mainprice, D. & Silver, P. G. (1993). Interpretation of SKS-waves using samples from the subcontinental lithosphere. *Physics of the Earth and Planetary Interiors* **78**, 257–280.

Mainprice, D., Humbert, M. & Wagner, F. (1990). Phase transformations and inherited lattice preferred orientation: Implications for seismic properties. *Tectonophysics* **180**, 213–228.

Mével, C. (2003). Serpentinization of abyssal peridotites at mid-ocean ridges. *Comptes Rendus de l'Académie des Sciences* **335**, 825–852.

Mével, C., Cannat, M., Gente, P., Marion, E., Auzende, J. M. & Karson, J. A. (1991). Emplacement of deep rocks on the west median valley wall of the MARK area. *Tectonophysics* **190**, 31–53.

Nicolas, A. & Poirier, J. P. (1976). *Crystalline Plasticity and Solid State Flow in Metamorphic Rocks*. London: John Wiley.

O'Hanley, D. S. (1996). *Serpentinites: Record of Tectonic and Petrologic History*. New York: Oxford University Press.

Richardson, R. M. (1992). Ridge forces, absolute plate motions, and the intraplates stress field. *Journal of Geophysical Research* **97**, 11739–11748.

Roden, M. F., Smith, D. & Murthy, V. R. (1990). Chemical constraints on lithosphere composition and evolution beneath the Colorado Plateau. *Journal of Geophysical Research* **95**, 2811–2831.

Rumori, C., Mellini, M. & Viti, C. (2004). Oriented, non-topotactic olivine → serpentine replacement in mesh-textured, serpentinized peridotites. *European Journal of Mineralogy* **16**, 731–741.

Smith, D. (1979). Hydrous minerals and carbonates in peridotite inclusions from the Green Knobs and Buell Park kimberlitic diatremes on the Colorado Plateau. In: Meyer, H. O. A. & Boyd, F. R. (eds) *The Mantle Sample: Inclusions in Kimberlites and Other Volcanics.* Washington, DC: American Geophysical Union, pp. 345–356.

Smith, D. (1995). Chlorite-rich ultramafic reaction zones in Colorado Plateau xenoliths: recorder of sub-Moho hydration. *Contributions to Mineralogy and Petrology* **121**, 185–200.

Swain, M. W. & Atkinson, B. K. (1978). Fracture surface energy of olivine. *Pure and Applied Geophysics* **116**, 866–872.